Rare Metal Materials and Engineering
Volume 50, Issue 11, November 2021
Available online at www.rmme.ac.cn

Science Press

Cite this article as: Yang Haifeng, Zhao Hongyun, Xu Xinxin, et al. Microstructure and Mechanical Properties of 2A14-T4 Aluminum Alloy T-joints Prepared by Stationary Shoulder Friction Stir Welding[J]. Rare Metal Materials and Engineering, 2021, 50(11): 3845-3856.

ARTICLE

Microstructure and Mechanical Properties of 2A14-T4 Aluminum Alloy T-joints Prepared by Stationary Shoulder Friction Stir Welding

Yang Haifeng[1,2], Zhao Hongyun[1,2], Xu Xinxin[2], Sun Guangda[1,2], Zhou Li[1,2], Zhao Huihui[3], Liu Huijie[1]

[1] State Key Laboratory of Advanced Welding and Joining, Harbin Institute of Technology, Harbin 150001, China; [2] Shandong Provincial Key Laboratory of Special Welding Technology, Harbin Institute of Technology (Weihai), Weihai 264209, China; [3] Shanghai Aerospace Equipments Manufacturer Co., Ltd, Shanghai 200245, China

Abstract: The 2A14-T4 Al-alloy T-joints were prepared by stationary shoulder friction stir welding (SSFSW) at different welding speeds. A smooth T-joint surface was obtained with the optimized welding process parameters. The results show that the microstructure of weld nugget zone (WNZ) consists of fine equiaxed grains caused by full dynamic recrystallization. The average grain size of the second weld nugget zone (WNZ2) is the largest, that of the weld nugget overlap zone (WNOZ) is in the middle, and that of the first weld nugget zone (WNZ1) is the smallest. The recrystallization mechanism in WNZ is mainly the geometric dynamic recrystallization accompanied by partial continuous dynamic recrystallization. The weak {100}<001> texture is formed in the WNOZ after two times of stirring, and the weak {111}<110> texture appears in WNZ1 and WNZ2. The thermo-mechanically-affected zone (TMAZ) undergoes plastic deformation, while the heat-affected zone (HAZ) is only affected by weld thermal cycles. No plastic deformation or the dynamic recrystallization of grains occurs in HAZ. The hardness of WNZ is high, and the zone with the lowest hardness is located in HAZ which is close to TMAZ. With increasing the welding speed, the ultimate tensile strength is firstly increased and then decreased. The mixed brittle/ductile fracture dominates the fracture mode of skin and stiffener plates.

Key words: 2A14-T4 aluminum alloy; SSFSW; T-joints; microstructure; mechanical properties

T-joints of aluminum alloys are widely used in aerospace, petrochemical, automobile, and agricultural equipment[1-3]. T-joints of aluminum alloys produced by riveting, extrusion forming, traditional fusion welding, and bonding manifest numerous drawbacks, such as restricted mold shape, high residual stress concentration, and burning loss of alloying elements[4,5]. Friction stir welding (FSW) is a novel solid-state bonding technique developed by The Welding Institute (TWI, UK) [6-8]. FSW has the advantages of easy processing, high welding joint quality, and low defect rate for welding the aluminum alloys[9-14]. FSW provides a new method for welding T-joints of aluminum alloys by converting T-joints into butt joints or lap joints using skin plates[15-17]. Excellent static mechanical properties can be obtained in previous studies[18-21]. However, there are a series of welding defects in FSW T-joints such as tunnel defect, bonding line defect, and Z-line defects[22-24].

Stationary shoulder friction stir welding (SSFSW) invented by TWI was firstly used to weld titanium alloys with low thermal conductivity and good welding quality was obtained[25,26]. The SSFSW system is mainly composed of a stationary shoulder and a stirring pin. A narrow thermo-mechanically-affected zone (TMAZ) and a uniformly thick heat-affected zone (HAZ) can be obtained as heat is generally produced around the stirring pin in the butt of SSFSW joint[27-29]. SSFSW also shows a high potential for fabricating corner and T-joints as welding is conducted from the inner side of the base skin, thus guaranteeing the integrity of the

Received date: March 15, 2021
Foundation item: Key National Defense Basic Research Project (JCKY2017203B066); National Natural Science Foundation of China (51974100); National Science and Technology Major Project (2017ZX04005001)
Corresponding author: Zhou Li, Ph. D., Associate Professor, Shandong Provincial Key Laboratory of Special Welding Technology, Harbin Institute of Technology (Weihai), Weihai 264209, P. R. China, Tel: 0086-631-5687196, E-mail: zhouli@hitwh.edu.cn

outer side of base skin[30,31]. Penalva et al[32] firstly proved the feasibility of welding T-joints by the SSFSW technique. However, the defects of tunnel, flashes, and grooves appeared in all welding processes, which was associated with the suck effect of tool on the stirred material. Numerical simulation was used to optimize the design of SSFSWed tool. The corresponding relationship between the temperature field distribution and groove defect in the SSFSWed T-joint was obtained by Buffa et al[33], which provided important information to optimize the design of SSFSW tool and the welding parameters. Gascoyne et al[34] found that the "blades" phenomenon is usually caused by the stir pin thread line in T-joint welding process through SSFSW method. But the impact of the "blades" phenomenon on the performance of the welding joint needs to be further investigated. Li et al[35] indicated that the welding speed and rotation speed are the key factors affecting the mechanical properties of T-joints prepared by SSFSW. The best strength coefficients of SSFSWed T-joint reach 78% and 96% in skin plate and the stiffener plate, respectively. It is worth noting that two times of welding processes are needed in the joining of T-joint by SSFSW technique. The annealing effect can be caused by the second welds on the previous welds. The residual stress peak and tensile regions are not symmetrically distributed in the preparation of SSFSWed T-joint[35,36].

The microstructure and mechanical properties of SSFSWed T-joints are greatly affected by tool design, temperature field distribution, and welding parameters. However, few researches discuss the new SSFSW process for T-joint fabrication. Therefore, further investigation for SSFSWed T-joints of aluminum alloy is needed. This research performed welding tests of SSFSWed T-joints of 2A14-T4 Al alloy and analyzed the temperature field distribution, the forming quality on the weld surface, the evolution of microstructures, and the related mechanical properties of alloys prepared at different welding speeds. The results provide the engineering application of 2A14-T4 Al alloy and the development of SSFSW process.

1 Experiment

The 2A14-T4 Al alloy was used as the base material (BM). The length, width, and thickness of skin plate were 300, 200, and 8.5 mm, and those of the stringer plate were 300, 100, and 8.5 mm, respectively. The chemical composition and mechanical properties of 2A14-T4 Al alloy are presented in Table 1.

A YXR33 tapered stirring pin with right-handed screw threads of ultra-high strength, high ductility, and excellent corrosion resistance was used to improve the material plasticity. Its length, root diameter, and front diameter were 92, 10.6, and 7.4 mm, respectively (Fig. 1a). Moreover, H13 steel was placed on the top of the stationary shoulder with the angle of 90° (Fig. 1b). Before welding, the skin plate and the stringer plate were fixed in a 90° fixture. Fig. 1c presents the overall assembly of the SSFSW system. The spacing between the stirring pin and the stationary shoulder was 0.3 mm. After the completion of the first welding process, the welded plate was taken out, overturned, and re-inserted into the fixture. The welded plate was naturally cooled for 1 h before the next welding process.

A gantry-type friction stir welding equipment was used in the experiment because of its easy operation. The main stationary angle was 0.5°. Table 2 shows the main parameters of the adopted welding process.

The metallographic specimen was cut from the welded joint by a wire-cut electric discharge machine and then eroded for 25~30 s by the standard Keller's reagent. The microstructures of different regions in cross section of T-joint were analyzed by an Olympus-DSX510 optical microscope (OM). The cross section of the metallographic specimen after corrosion was analyzed by an ARTCAN-300SSI-C microhardness tester (Fig. 2). Feature data points along two directions were plotted, and two measuring points of 3.5 mm above the floor and at the centerline of the stringer plate were selected. The spacing between these two measuring points was 0.5 mm. Fig. 3c displays the dimensions of the tensile specimen, and the test load and the pressure-holding time were set as 0.98 N and 15 s, respectively. The specimen was tested along the axial direction of the skin plate and the stringer plate by the INSTRON 5967 electronic universal material tester at a loading rate of 5 mm/min. A scanning electron microscope (SEM, TESCAN VEGAII) was used to analyze the fracture surface morphology and constituent particle distribution of the welded joints. Electron backscattered diffraction (EBSD) was performed to investigate the texture of the SSFSWed T-joint. EBSD images were obtained by a field-emission SEM (FE-SEM). Grain orientation maps, grain boundary maps, and pole figures (PFs) were plotted by OIMTM software.

The distribution of the temperature field in SSFSWed T-joints was used in the commercial finite element analyzer software ABAQUS. Considering the complex thermodynamic variation during the welding process, the plastic deformation heat of materials and the latent heat of phase change during the structural transformation were ignored, and only the friction heat was taken into consideration[37-40]. The simulated geometrical model mainly consisted of two parts: the materials to be welded and the shaft shoulder. The entire welding process could be simplified as follows: enhance the computational speed and satisfy the requirement of model convergence. By neglecting the characteristics of the upper

Table 1 Chemical composition and mechanical properties of 2A14-T4 aluminum alloy

Chemical composition/wt%									Mechanical properties		
Fe	Cu	Mg	Si	Zn	Ti	Ni	Mn	Al	Tensile strength/MPa	Elongation/%	Microhardness, HV/MPa
0.7	3.9~4.8	0.4~0.8	0.6~1.2	0.3	0.15	0.1	0.4~1.0	Bal.	420	15~17	1200~1250

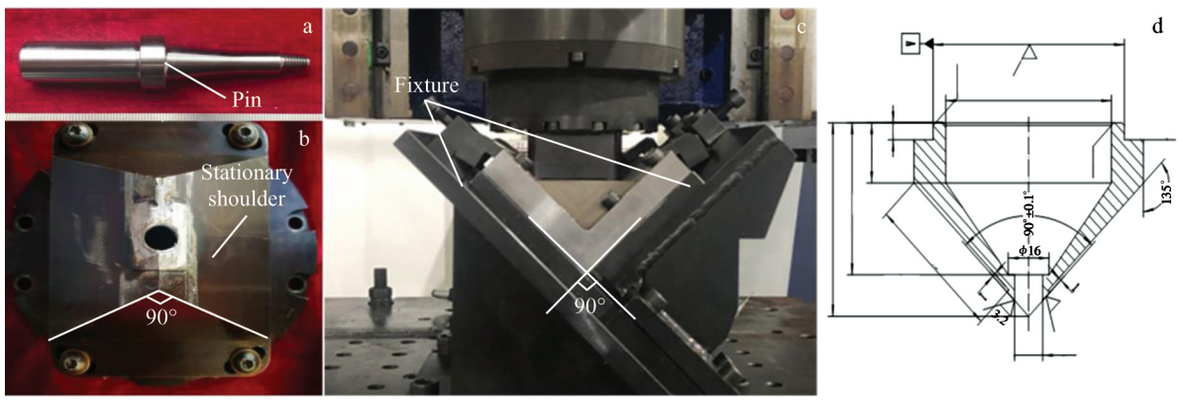

Fig.1 Appearances of SSFSW tools for T-joint fabrication: (a) stirring pin, (b) stationary shoulder, and (c) welding fixture assembly; schematic diagram of welding fixture assembly (d)

Table 2 SSFSW process parameters for preparation of 2A14-T4 alloy T-joints at rotation speed of 2000 r/min

Specimen	Welding speed/mm·min^{-1}	Pass
1	25	1st
2		2nd
3	50	1st
4		2nd
5	75	1st
6		2nd
7	100	1st
8		2nd

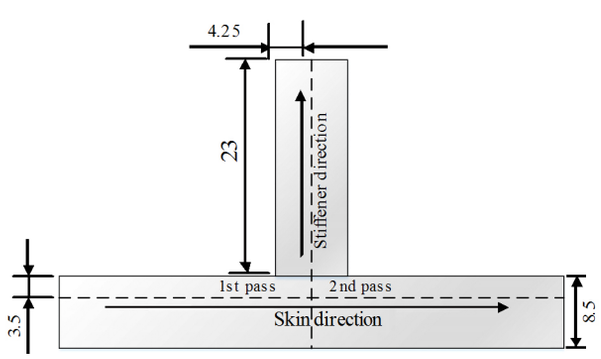

Fig.2 Schematic diagram of microhardness test for T-joints of 2A14-T4 alloy

part of the shaft shoulder, only the lower part of the shaft shoulder and the adhesive part of the to-be-welded materials were considered in calculations.

To optimize the computations, several different types of meshes were adopted. The to-be-welded material was meshed using 8-node linear-heat-transfer hexahedral elements DC3D8. Fine structural meshes were generated near the weld zone, sparse meshes were generated far away from the weld zone, and transitional meshes with the size from 1 mm×1 mm to 5 mm×5 mm were generated in the middle. In general, 61 143 mesh elements in total were generated in the to-be-welded material. Besides, uniform meshes were generated in the stationary shoulder using 10-node secondary-heat-transfer tetrahedron elements DC3D10, considering that no heat was produced during the welding process. 1098 meshes in total were generated in the shoulder part. Fig. 4 shows the mesh generation results. The temperature change at feature point located at 20 mm away from the welding center along the skin and stiffener plate directions during the welding process was measured by a WZ-CP16 multi-channel temperature meter and the GG-K-30 thermocouples.

2 Results and Discussion

2.1 Distribution characteristics of temperature field in SSFSWed T-joints

Fig.5 shows the comparison between the simulated thermal cycle curves and the measured results of SSFSWed T-joints prepared at a rotation speed of 2000 r/min and a welding speed of 50 mm/min. Only the temperature distribution field in the first pass is considered, because the second pass has a nearly identical temperature distribution pattern with the first welds. The simulated peak temperatures on the advancing side (AS) and the retreating side (RS) exceed the measured data by approximately 5 °C, suggesting that the simulation results fit well with the measured data in terms of temperature variation rate and temperature value.

It can also be observed that during the welding process, the stirring pin is subjected to the material resistance in the forward process, and the heat produced in friction accumulates rapidly. As the stirring pin moves closer to the thermocouple-measured region, its heat grows faster than the heat of insertion phase does. When the stirring point moves to the closest position to the temperature-meter-measured region, the peak temperature can be obtained. Afterward, the stirring pin continues to move forward, getting further away from the thermocouple-measured region. No sufficient heat can be transferred from the stirring pin to the measured region for

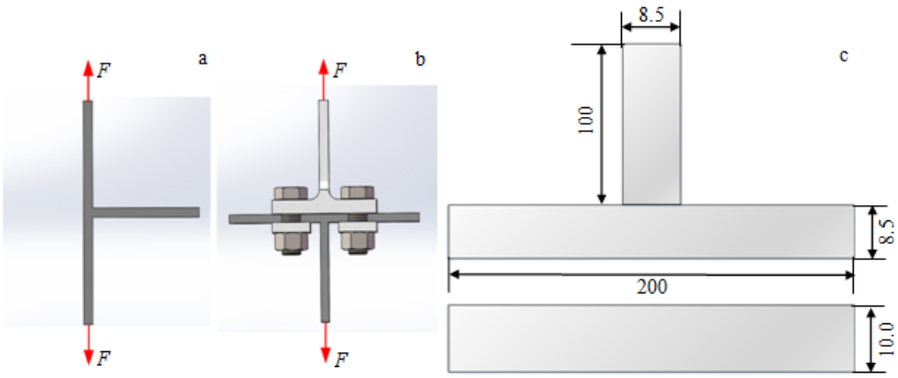

Fig.3 Schematic diagrams of tensile loading of SSFSWed T-joints along skin (a) and stiffener (b) plate directions; dimension of tensile specimen (c)

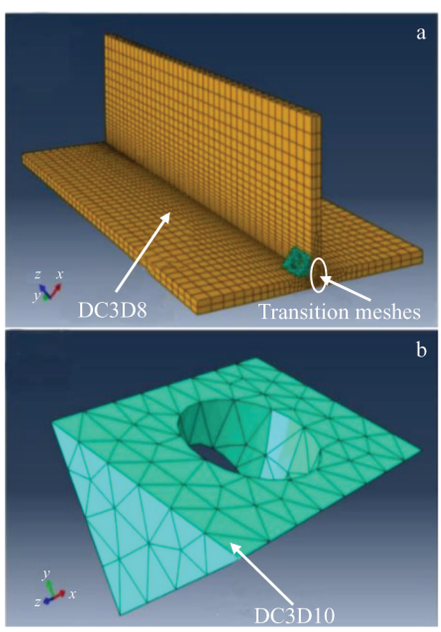

Fig.4 Mesh generation results of geometrical model: (a) to-be-welded material and (b) stationary shoulder

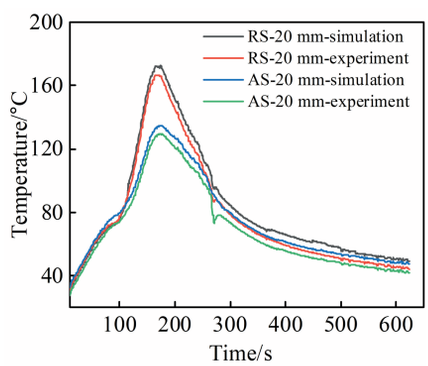

Fig.5 Comparison between simulated thermal cycle curves and measured results of SSFSWed T-joints prepared at rotation speed of 2000 r/min and welding speed of 50 mm/min

sustaining the heat dissipation in the thermocouple-measured region, thereby leading to a temperature drop. The peak temperatures at the AS and RS are not completely symmetrical. Specifically, the peak temperature at the AS is 80.6% of that at the RS. This is because the material on the front side is subjected to shear extrusion and gradually rotated to the rear side, causing the material accumulation and higher peak temperature on the RS. Meanwhile, the inconsistency of heat dissipation condition also accelerates the non-uniformity of the peak temperature distribution on two sides.

Fig. 6 depicts the conditions of the stable welding phase at different welding speeds. It can be seen that the temperature fields at the feature point extend towards two sides in the elliptical area around the weld. The isothermal lines are densely distributed in front of the heat source with a great temperature gradient. In contrast, the isothermal lines at the back of the source are sparsely distributed with a small temperature gradient. The high-temperature region is located at the contact center between the stirring center and the welded material. Under the fixed rotation speed, the increase in welding speed leads to the decrease in friction-induced heat between the stirring pin and the to-be-welded material. Accordingly, the thermal input per unit time also drops, decreasing the peak temperature value.

2.2 Surface morphology of SSFSWed T-joints

Fig. 7 displays the surface morphologies of SSFSWed T-joints after 1st and 2nd passes at different welding speeds. The stationary shoulder slides over the joint surface, and it plays a cooling effect on the joint and acts as a heat sink. Furthermore, the stationary shoulder acts as a “sealed barrier” and effectively prevents the plastic material from flowing out of the joint. Thus, the “arc line” phenomenon can be avoided. It is observed from Fig. 7 that SSFSWed T-joints without grooves can be obtained after both 1st and 2nd passes of process at relatively lower welding speeds (25 and 50 mm/min). However, the groove size of the SSFSWed T-joints increases after 1st and 2nd passes of process at higher welding speeds (75 and 100 mm/min). This is because the heat input is decreased, the viscosity of the plastic material becomes

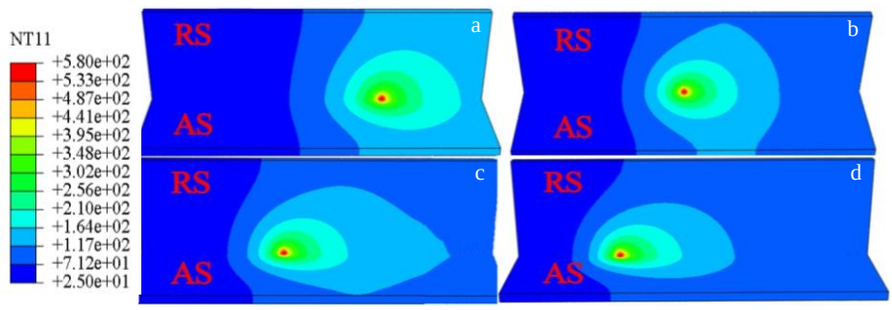

Fig.6 Distributions of temperature fields in stable welding process using different welding speeds: (a) 25 mm/min, (b) 50 mm/min, (c) 75 mm/min, and (d) 100 mm/min

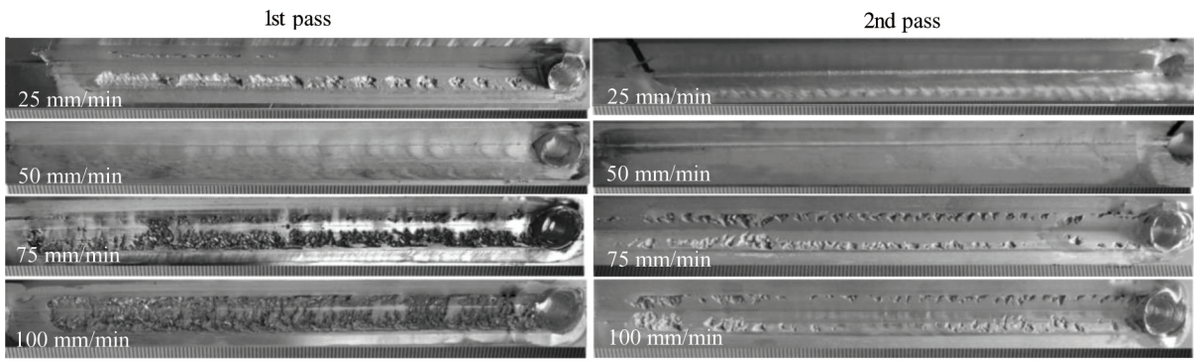

Fig.7 Surface morphologies of SSFSWed T-joints after 1st and 2nd passes at different welding speeds

smaller, and the flow of material gets slower with increasing the welding speed. Furthermore, the material cannot be back-filled to AS in time due to the "sucking effect"[28], leading to the fact that the groove defects are more obvious on AS than those on RS. In brief, SSFSWed T-joints of 2A14-T4 aluminum alloy show a smooth surface without shoulder marks or flashes under the optimized welding process parameters. The surfaces of T-joints prepared at different welding speeds are quite different.

2.3 Microstructure analysis

The appearance and inverse pole figures (IPFs) with the information of misorientation angle distributions and mean grain size distributions of SSFSWed T-joint prepared at a rotation speed of 2000 r/min and a welding speed of 50 mm/min are shown in Fig. 8 and Fig. 9, respectively. The overall cross section of the weld nugget zone (WNZ) is slightly different from that of traditional FSWed material. WNZ has an "open dumbbell" shape with two wide ends and a narrow middle zone. Threads on the stirring pin increase the fluidity of the material during welding. A prominent "onion ring" can be detected in the center of WNZ. According to the welding characteristics of SSFSWed T-joints, WNZ can be divided into the first weld nugget zone (WNZ1), the second weld nugget zone (WNZ2), and the weld nugget overlap zone (WNOZ)[32]. Moreover, the TMAZ is narrow, and its variation trend is consistent with that of the shape of WNZ.

It is evident from Fig. 9 that the material in WNZ is

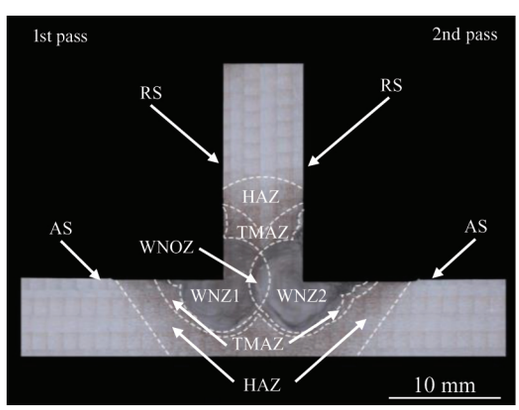

Fig.8 Cross section of SSFSWed T-joint prepared at rotation speed of 2000 r/min and welding speed of 50 mm/min

subjected to violent stirring by the stirring pin and the original structure undergoes an intense thermo-mechanical action, leading to the recovery and recrystallization of WNZ grains. Moreover, WNZ consists of fine equiaxed grains. The mean grain sizes in WNZ1, WNOZ, and WNZ2 are 4.01, 4.39, and 5.80 μm, respectively. The deformation in the first pass reduces the heat conduction efficiency of the stirring pin during the second pass, which thereby fails to provide sufficient heat in time and significantly weakens the recrystallization degree of grains in this region after welding.

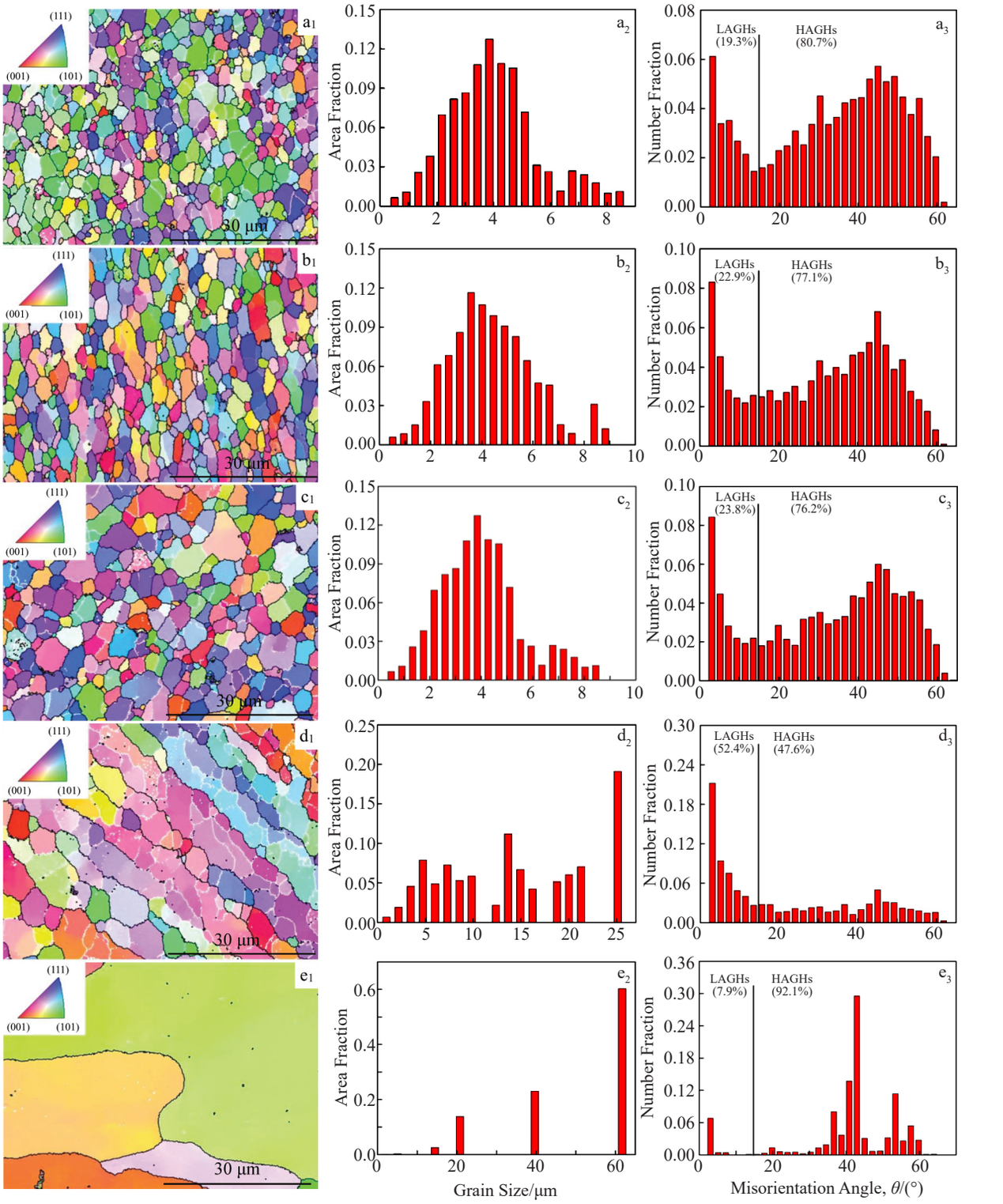

Fig.9 IPFs (a_1~e_1), main grain sizes (a_2~e_2), and misorientation angle distributions (a_3~e_3) of different zones in SSFSWed T-joints prepared at rotation speed of 2000 r/min and welding speed of 50 mm/min: (a_1~a_3) WNZ1, (b_1~b_3) WNOZ, (c_1~c_3) WNZ2, (d_1~d_3) TMAZ, and (e_1~e_3) HAZ

Furthermore, WNZ is dominated by high-angle grain boundaries (HAGBs) with a high proportion of approximate 78%, meeting the condition of geometric dynamic recrystallization (GDRX)[30]. Moreover, numerous mesh sub-boundaries can be observed in grains, and some sub-boundaries rotate and become entangled. As numerous dislocations are produced under severe plastic deformation, dislocations with a small spacing can easily form a dislocation wall after weld thermal cycles. Hence, by applying the external force, the sub-boundaries constantly rotate and absorb the dislocation energy

to form HAGBs, meeting the conditions of continuous dynamic recrystallization (CDRX)[30]. Hence, the recrystallization mechanism in WNZ is dominated by GDRX accompanied by CDRX.

Furthermore, TMAZ is subjected to a shear action induced by the material plastic flow around the stirring pin and by the weld thermal cycles to a certain degree during the welding process. Consequently, the grains become elongated and are deformed along the direction of the maximum shear force. The mean grain size in TMAZ is 14.44 μm. The proportion of HAGBs in TMAZ is only 47.6%, which is significantly decreased, compared with that in WNZ. Therefore, it can be inferred that the distortion energy in TMAZ is too low for recrystallization.

Grains in HAZ is coarsened to a certain degree under weld thermal cycles. A large number of low-angle grain boundaries (LAGBs) appear in HAZ. Therefore, the grain thickness begins to decrease and the sub-structures start to appear in grains. The mean grain size and the proportion of HAGBs are 50.40 μm and 92.1%, respectively. As HAZ is only subjected to weld thermal cycles during the welding process, the energy is gradually increased and it promotes the dislocation propagation and entanglement. Subsequently, the LAGBs constantly absorb the surrounding dislocations and form HAGBs. Grains in HAZ are flat with a high rotation density of sub-structures. No dynamic recrystallization occurs in the HAZ region.

The texture characteristics of SSFSWed T-joints prepared at a rotation speed of 2000 r/min and a welding speed of 50 mm/min are presented in Fig.10. The texture of WNZ is weak.

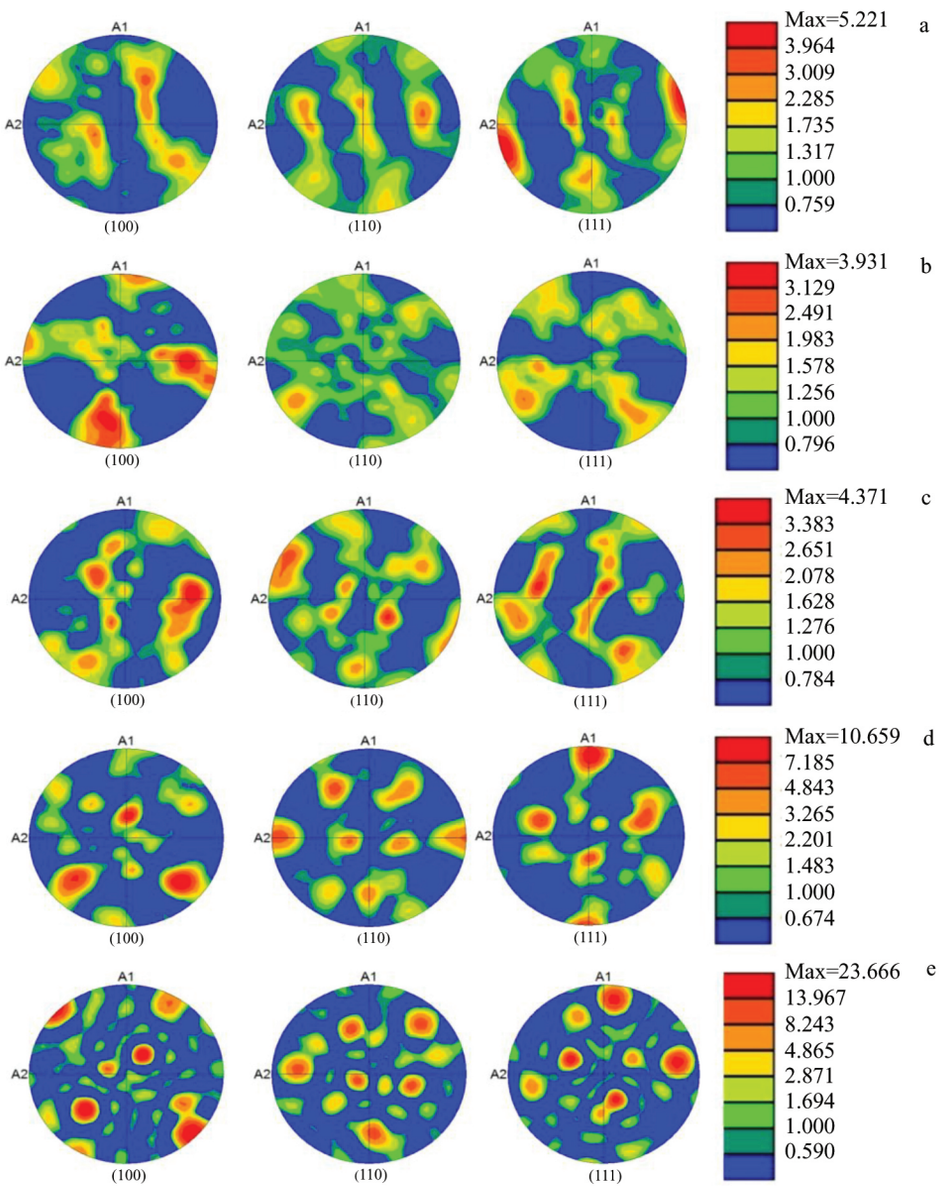

Fig.10 PFs of different zones in SSFSWed T-joint prepared at rotation speed of 2000 r/min and welding speed of 50 mm/min: (a) WNZ1, (b) WNOZ, (c) WNZ2, (d) TMAZ, and (e) HAZ

The mean maximum pole density of three WNZs is only 4.490, suggesting the great disorderliness. The texture type in WNOZ changes significantly, compared with that in WNZ1 and WNZ2. A weak {100}<001> cubic texture is formed in WNOZ, whereas a weak {111}<110> texture appears in both WNZ1 and WNZ2. As the orientation factor of the (111) plane along [110] direction is the lowest and the T-joint is subjected to the mechanically stirring action twice, the grains have a high recrystallization degree in WNOZ and show the orientation disorder. The maximum pole density of TMAZ is 10.659. Moreover, TMAZ undergoes plastic deformation and has a strong {112}<111> texture. The maximum pole density of HAZ is 23.666 and has a typical {110}<001> texture, indicating that HAZ is recovered during weld thermal cycles.

Fig.11 displays the microstructures and mean grain sizes of T-joints at different welding speeds. It is noticeable that the mean grain sizes in WNZ and TMAZ are decreased with increasing the welding speed. In WNZ, as the welding speed increases, the material is subjected to a lower stirring action, reducing the deformation rate of the material, weakening the recrystallization degree, and resulting in grain coarsening. Moreover, the increasing welding speed leads to a decline of the thermal input. Thus, the deformation temperature drops significantly and the grain growth is suppressed. These two actions occur simultaneously as the welding speed is increased from 25 mm/min to 100 mm/min. However, the thermal input plays a key role in determining the final grain size. As the thermal input drops steadily, the grain growth in WNZ becomes increasingly difficult and the mean grain size in WNZ gradually decreases. During the stirring action, TMAZ is elongated. Moreover, the increasing welding speed weakens the stirring action and the elongation of grains. The reduction of the thermal input also decreases the deformation temperature and the mean grain size.

The mean grain size in HAZ is firstly increased and then decreased with increasing the welding speed. The thermal input of HAZ only drops slightly and is still high as the welding speed is increased from 25 mm/min to 50 mm/min, compared with that of WNZ. On the contrary, the strain rate drops noticeably, resulting in the partial grain growth. As the welding speed further increases, the thermal input drops greatly, which seriously suppresses the grain growth, thereby decreasing the mean grain size.

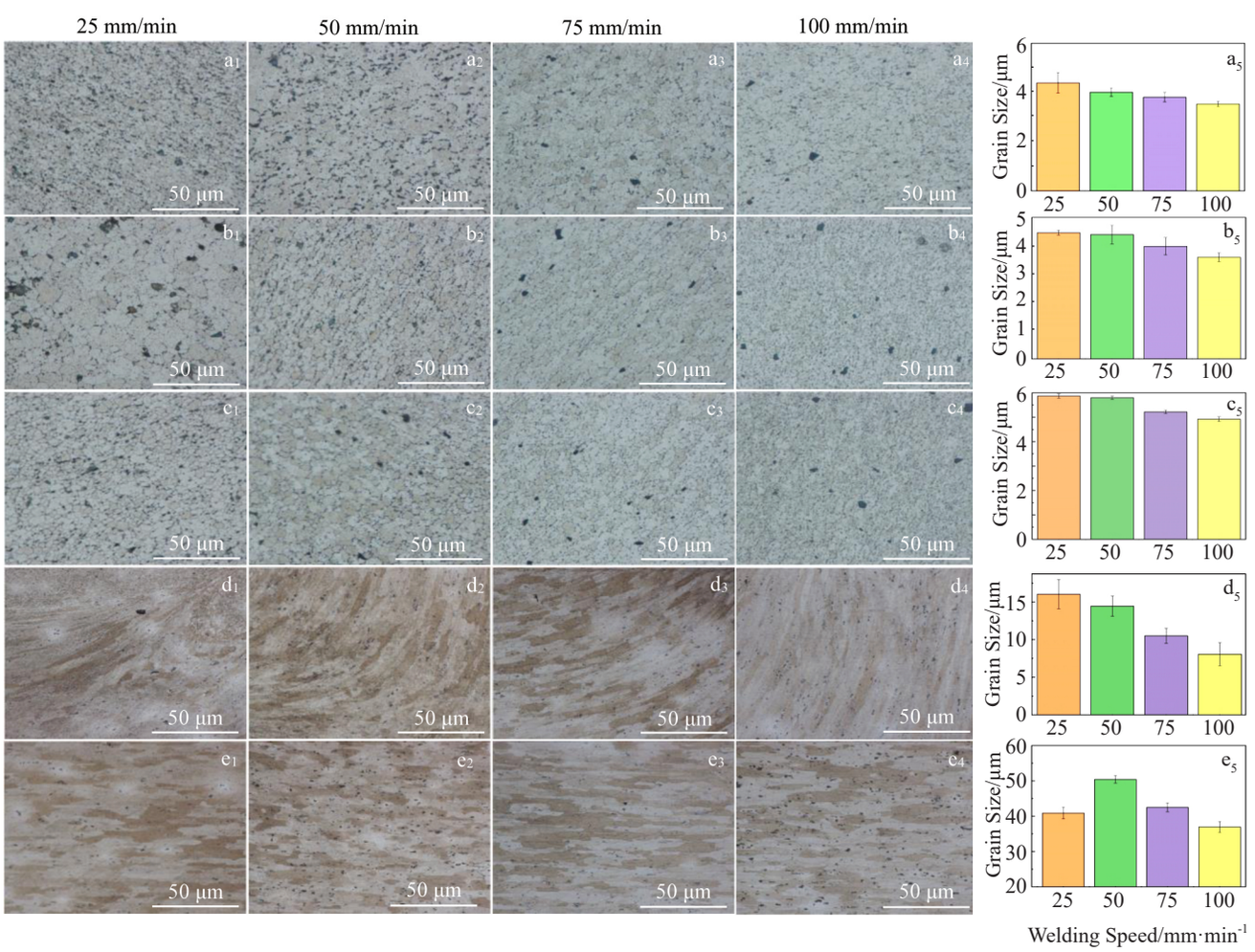

Fig.11 Microstructures (a_1~a_4, b_1~b_4, c_1~c_4, d_1~d_4, e_1~e_4) and mean grain sizes (a_5~e_5) of different zones in SSFSWed T-joints at different welding speeds: (a_1~a_5) WNZ1, (b_1~b_5) WNOZ, (c_1~c_5) WNZ2, (d_1~d_5) TMAZ, and (e_1~e_5) HAZ

2.4 Properties of SSFSWed T-joints

2.4.1 Microhardness

Fig. 12 displays the microhardness change trend along the directions of the skin plate and the stiffener plate. The overall microhardness distribution along the skin plate is W-shaped. The zone with the lowest microhardness is located in HAZ which is close to the TMAZ boundary. Recovery and incomplete dynamic recrystallization occur in TMAZ. Consequently, the elongated grains of different sizes are formed. Thus, the microhardness of TMAZ is higher than that of HAZ. Moreover, HAZ is only affected by the welding temperature field, and grains are coarsened with an obvious decrease of microhardness. The overall microhardness distribution in the stiffener plate is N-shaped. The zone with the lowest microhardness is also located in HAZ which is close to the TMAZ boundary.

Precipitation is the main strengthening factor of the 2A14-T4 Al alloy. Fig. 13 displays the temperature change trends in the WNZ and TMAZ at different welding speeds. As the welding speed is increased from 25 mm/min to 100 mm/min, the peak temperature in the WNZ is decreased from 578.2 °C to 481.6 °C; the peak temperature in TMAZ is decreased linearly from 340.3 °C to 267.5 °C at a significantly lower temperature decreasing rate than the value in WNZ. The peak temperature of WNZ is higher than the solid-solution temperature of precipitations. The original $CuAl_2$ phase is fully recovered, whereas the α solid-solution is partly recovered. In the subsequent cooling process, atoms are reorganized into reprecipitated phases. The microhardness of WNZ1 is slightly lower than that of WNZ2, which can be attributed to the growth and coarsening of precipitated phases

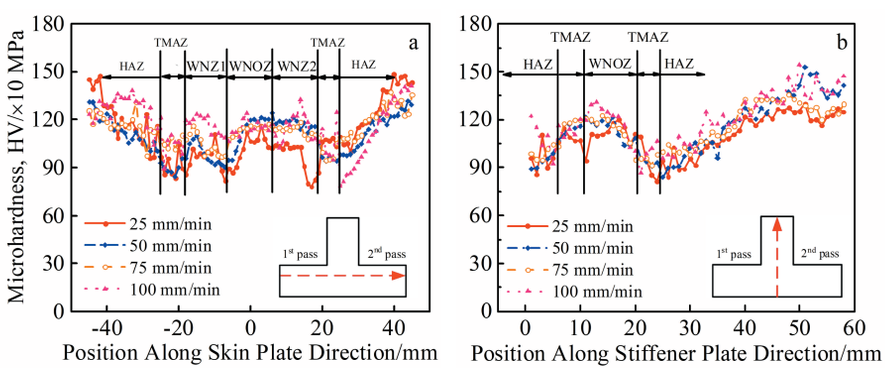

Fig.12 Microhardness change trends of SSFSWed T-joints with different welding speeds along skin (a) and stiffener (b) plate directions

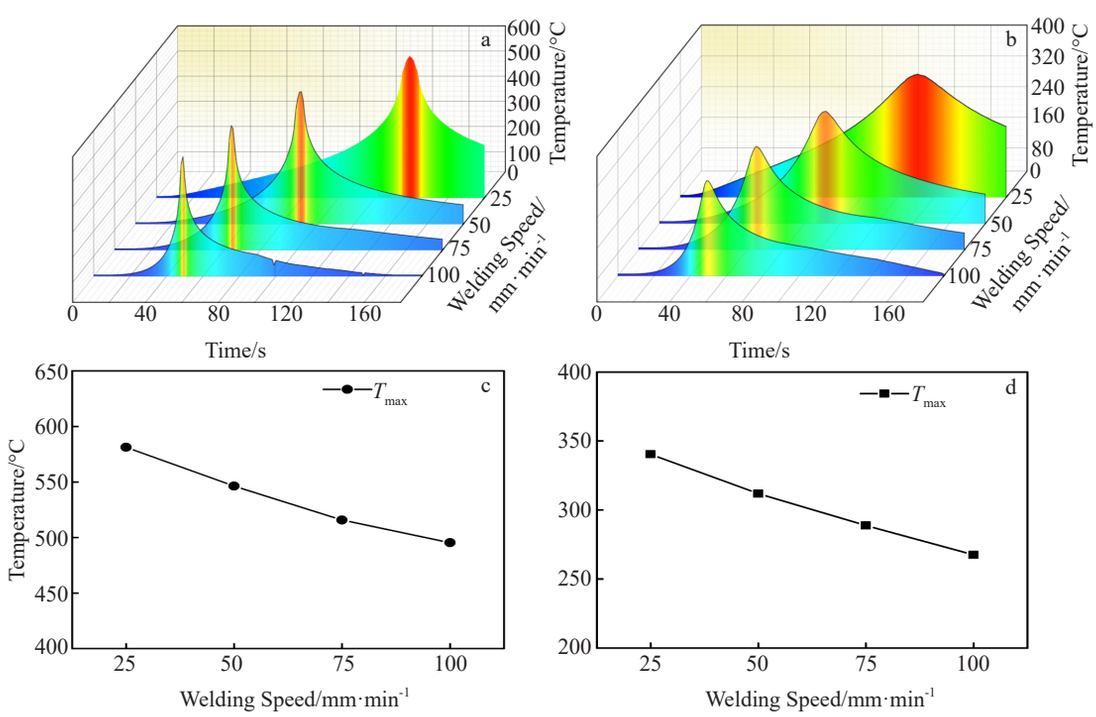

Fig.13 Temperature change in WNZ (a, c) and TMAZ (b, d) of welded T-joints at different welding speeds

in WNZ1 by the thermal input during 2nd welding process. The welding peak temperatures of TMAZ and HAZ are lower than the solid-solution temperature of precipitations. Under the effect of thermal cycling, the precipitates grow and become coarse. Therefore, the minimum microhardness of HAZ can be obtained near TMAZ. No prominent difference can be noticed in the microhardness distributions along the skin plate direction or the stiffener plate direction with increasing the welding speed. With increasing the welding speed, the microhardness is increased slightly along both the directions of skin and stiffener plates. This is because the heat input decreases and the content of precipitated phase in the T-joints relatively increases, which leads to the slight increase in microhardness.

2.4.2 Tensile strength

The ultimate tensile strength (UTS) of BM and SSFSWed T-joints along the skin plate and the stiffener plate directions is presented in Fig. 14. With increasing the welding speed, UTS of the SSFSWed T-joints is firstly increased and then decreased along both the skin and stiffener plate directions.

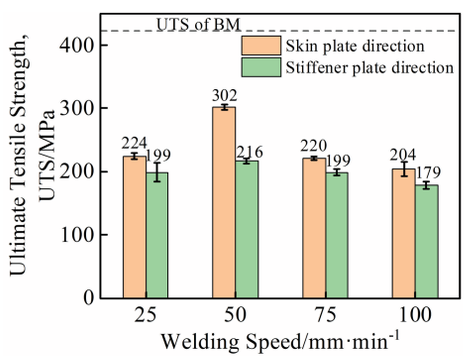

Fig.14 UTS of BM and SSFSWed T-joints along skin plate and stiffener plate directions

This is because with increasing the welding speed from 25 mm/min to 50 mm/min, the heat dissipation effect of the welding zone is increased obviously, while the degree of plastic deformation of material near the pin is also increased. So the proportion of plastic deformation increases, leading to the improvement of the mechanical properties of the welding area. However, when the welding speed is too fast, such as 75~100 mm/min, the heat input of the weld per unit length is decreased, the plastic deformation of the material becomes worse, and the plastic material has no time to backfill the weld, resulting in groove defects on the weld surface and the decline in UTS of the T-joints[41-43]. The maximum UTS is 302 and 216 MPa for the SSFSWed T-joint prepared at rotation speed of 2000 r/min and welding speed of 50 mm/min along the skin and stiffener plate directions, which is about 71.21% and 50.93% of the UTS value of the BM, respectively. Thus, the SSFSWed T-joints show good mechanical properties.

2.5 Fracture morphology

The fracture morphologies along the skin plate direction at different welding speeds are shown in Fig. 15. When the welding speed is slow, the tearing edges and dimples of different sizes appear in the crack growth area and a small number of dissociation platforms appear in the fiber area. When the welding speed increases to 50 mm/min, the smaller secondary phase particles appear in the dimples. Consequently, the dimples become deeper and are located in the crack propagation zone, indicating that the plasticity is significantly improved. When the welding speed continues to increase, the secondary phase particles grow into dimples. A small amount of plastic deformation separates these particles from the substrate, which forms pores and cracks. These defects greatly reduce the plastic deformation capacity and lead to a decline in toughness. Moreover, the cleavages and numerous secondary cracks can be observed in the transient fault surface, indicating the poor crack propagation resistance.

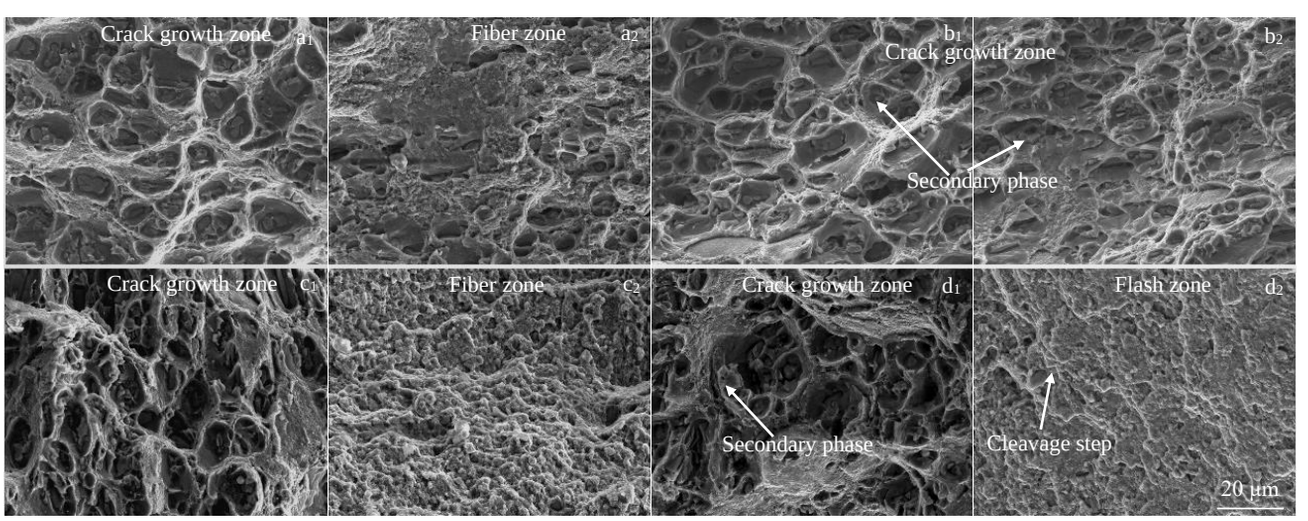

Fig.15 Fracture morphologies of SSFSWed T-joints along skin plate direction at different welding speeds: (a_1, a_2) 25 mm/min, (b_1, b_2) 50 mm/min, (c_1, c_2) 75 mm/min, and (d_1, d_2) 100 mm/min

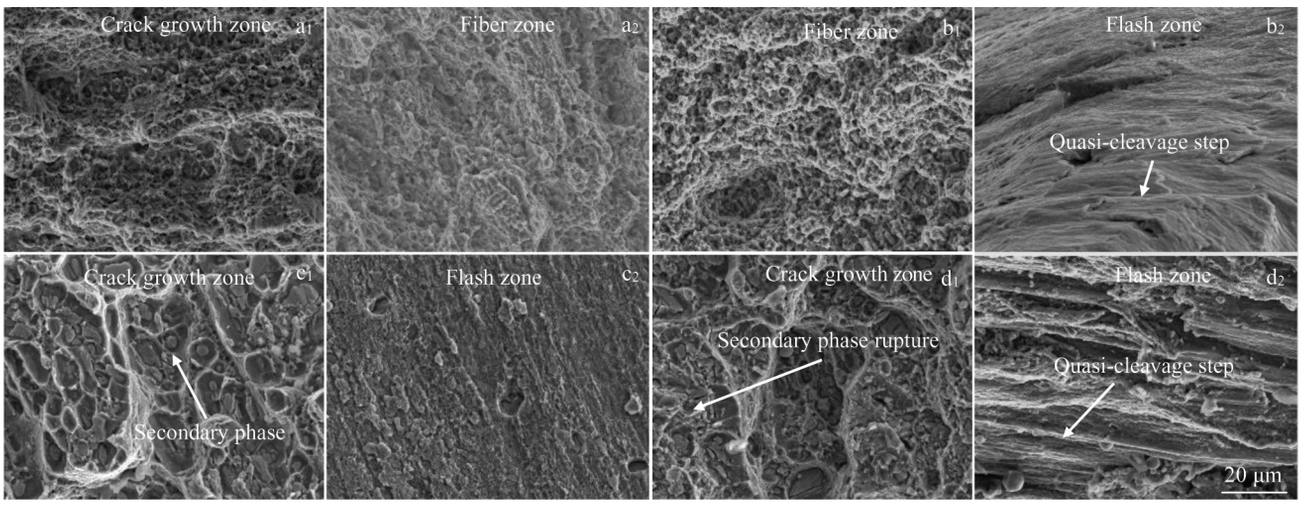

Fig.16 Fracture morphologies of SSFSWed T-joints along stiffener plate direction at different welding speeds: (a_1, a_2) 25 mm/min, (b_1, b_2) 50 mm/min, (c_1, c_2) 75 mm/min, and (d_1, d_2) 100 mm/min

With increasing the welding speed, the fracture mode gradually changes from ductile fracture to the mixed ductile/brittle fracture.

The fracture morphologies along the stiffener plate direction at different welding speeds are presented in Fig. 16. When the welding speed is slow, the dimple size is small. When the welding speed increases to 50 mm/min, the fracture surface is covered with a large number of continuous fine dimples. However, a few quasi-cleavage steps appear at the bottom of the fracture zone. When the welding speed is 75 mm/min, the grain boundary deformation is serious and a large number of secondary phase particles in the dimples peel off as the number of dimples is significantly reduced. When the welding speed increases to 100 mm/min, the dimple is shallow and the grain boundary deformation is more serious. A large number of secondary cracks, secondary phase particles, and quasi-cleavage steps appear, leading to the decrease of the plastic deformation ability of the material. With increasing the welding speed, the fracture mode of the T-joints along the stringer plate direction changes from micropore aggregation fracture to the mixed ductile/brittle fracture mode. As the welding speed increases, the mixed brittle/ductile fracture dominates the fracture of skin plate and the stiffener plate.

3 Conclusions

1) T-joints of 2A14-T4 aluminum alloy after stationary shoulder friction stir welding (SSFSW) show a smooth surface without shoulder marks or flashes under the optimized welding process parameters. The surfaces of T-joints prepared at different welding speeds are quite different.

2) The SSFSWed T-joints have an open-dumbbell morphology with two wide ends and a narrow middle zone. The texture of weld nugget zone (WNZ) is weak because both the first weld nugget zone (WNZ1) and the second weld nugget zone (WNZ2) have the {111} <110> shear texture; whereas the texture type of the weld nugget overlap zone (WNOZ) is transformed into a {100}<001> cubic texture after two welding passes.

3) The microhardness change trends can be characterized as “W” and “N” shapes along the skin plate and stiffener plate directions, respectively. The zone with the lowest microhardness is located in heat-affected zone (HAZ) which is close to the thermo-mechanically-affected zone (TMAZ) boundary, resulting in an annealing effect of the second weld on the previous weld.

4) The maximum ultimate tensile strength (UTS) is firstly increased and then decreased with increasing the welding speed. The fracture morphology consists of deformed dimples of different sizes, and the second phase particles can be found in these dimples.

References

1 Sun Hongye, Cong Baoqiang, Qi Zewu *et al*. *Rare Metal Materials & Engineering*[J], 2017, 46(8): 2203 (in Chinese)
2 Liu D J, Xin R L, Zheng X *et al*. *Materials Science & Engineering A*[J], 2013, 561(1): 419
3 Zou Dongli, Chen Xianglin, Xiao Dawu *et al*. *Rare Metal Materials & Engineering*[J], 2019, 48(9): 2951 (in Chinese)
4 Gao Wenlin, Ban Chunyan, Cui Jianzhong *et al*. *Rare Metal Materials & Engineering*[J], 2019, 48(4): 1155 (in Chinese)
5 Ma Z Y, Sharma S R, Mishra R S. *Materials Science & Engineering A*[J], 2006, 433(1-2): 269
6 Liu Jingxuan, Shen Jian, Li Xiwu *et al*. *Rare Metal Materials & Engineering*[J], 2019, 48(12): 3797
7 Mishra R S, Ma Z Y. *Materials Science & Engineering*[J], 2005, 50(1-2): 1
8 Kah P, Rajan R, Martikainen J *et al*. *International Journal of Mechanical & Materials Engineering*[J], 2015, 10(1): 1
9 Gibsona B T, Lammlein D H, Prater T J *et al*. *Journal of*

Manufacturing Processes[J], 2014, 16(1): 56
10 Meng Xiangchen, Huang Yongxian, Cao Jian *et al*. *Progress in Materials Science*[J], 2021, 115: 100 706
11 Yu Zhongliang, Zhao Yongqing, Zhou Lian *et al. Rare Metal Materials & Engineering*[J], 2009, 38(2): 224 (in Chinese)
12 Dumont D, Deschamps A, Brechet Y. *Materials Science & Engineering A*[J], 2003, 356(1-2): 326
13 Miller W S, Zhuang L, Bottema J *et al*. *Materials Science & Engineering A*[J], 2000, 280(1): 37
14 Chen Xiangrong, Zheng Ziqiao, Ye Zhihao *et al*. *Rare Metal Materials & Engineering*[J], 2018, 47(6): 1786 (in Chinese)
15 Hou Xiaopeng, Yang Xinqi, Cui Lei *et al*. *The Chinese Journal of Nonferrous Metals*[J], 2013, 23(11): 3048 (in Chinese)
16 Fratini L, Buffa G, Shivpuri R. *Materials & Design*[J], 2009, 30(7): 2435
17 Donati L, Tomesani A, Morri A. *International Journal of Material Forming*[J],2009, 2(S1): 295
18 Acerra F, Buffa G, Fratini L *et al*. *The International Journal of Advanced Manufacturing Technology*[J], 2010, 48(9-12): 1149
19 Cui L, Yang X Q, Xie Y H *et al*. *Materials & Design*[J], 2013, 51: 161
20 Schmidt H, Hattel J. *Modelling & Simulation in Materials Science & Engineering*[J], 2004, 13(1): 77
21 Zhou Guang, Yang Xinqi, Xu Xiaodong *et al*. *Journal of Aeronautical Materials*[J], 2012, 32(4): 26 (in Chinese)
22 Fratini L, Micari F, Squillace A *et al*. *Key Engineering Materials* [J], 2007, 344(2): 751
23 Hou X P, Yang X Q, Cui L *et al*. *Materials & Design*[J], 2014, 53(1): 106
24 Zhao Y, Zhou L L, Wang Q Z *et al*. *Materials & Design*[J], 2014, 53(1): 106
25 Sun T, Roy M J, Strong D *et al*. *Journal of Materials Processing Technology*[J], 2017, 242: 92
26 Ahmed M, Wynne B P, Rainforth W M *et al*. *Scripta Materialia* [J], 2011, 64(1): 45
27 Wu H, Chen Y C, Strong D *et al*. *Journal of Materials Processing Technology*[J], 2015, 221: 187
28 Krasnowski K. *Arabian Journal for Science & Engineering*[J], 2014, 39(12): 9083
29 Li D, Yang X, Cui L *et al*. *Journal of Materials Processing Technology*[J], 2015, 222(1): 391
30 Martin J P. *Proceedings of 1st International Joint Symposium on Joining & Welding*[C]. Osaka: Woodhead Publishing, 2013: 477
31 Ji Hua, Xu Meng, Feng Xiaosong *et al*. *Electric Welding Machine*[J], 2013, 43(9), 37 (in Chinese)
32 Penalva M L, Otaegi A, Pujana J *et al*. *AIP Third Manufacturing Engineering Society International Conference*[C]. Alcoy: American Institute of Physics[J], 2009: 1
33 Buffa G, Fratini L, Arregi B *et al*. *International Journal of Material Forming*[J], 2010, 3(S1): 1039
34 Gascoyne J S. *A Microstructural Investigation into the Stationary Shoulder Corner Friction Stir Welding of Aluminum Alloys*[D]. Sheffield: University of Sheffield, 2014
35 Li Dongxiao. *Study of Stationary Shoulder Friction Stir Welding of Aluminum Alloy*[D]. Tianjin: Tianjin University, 2015 (in Chinese)
36 Sun T, Roy M J, Strong D *et al*. *Journal of Materials Processing Technology*[J], 2019, 263: 256
37 Liu Qipeng, Gu Naijian, Liu Ze *et al. Journal of Dalian Jiaotong University*[J], 2018, 39(3): 80 (in Chinese)
38 Schmidt H, Hattel J, Wert J. *Modelling & Simulation in Material Science & Engineering*[J], 2004, 12(1): 143
39 Khandkar M Z H, Khan J A, Reynolds A P. *Science & Technology of Welding & Joining*[J], 2003, 8(3): 165
40 Gadakh V S, Kumar A. *Journal of Materials Research & Technology*[J], 2013, 2(4): 370
41 Zhang Renxiao. *Research on Microstructure Evolution & Properties of Friction Stir Processed 2507 Duplex Stainless Steel* [D]. Harbin: Harbin Institute of Technology, 2019 (in Chinese)
42 Wang Yaobin. *The Study of Friction Stir Processing on Microstructural Evolution & Strengthening & Toughening of Mg-Zn-Y-Zr Alloy*[D]. Harbin: Harbin Institute of Technology, 2017 (in Chinese)
43 Chen J, Fujii H, Sun Y *et al. Journal of Materials Processing Technology*[J], 2017, 242: 117

2A14-T4铝合金T形接头静轴肩搅拌摩擦焊组织结构与力学性能

杨海峰[1,2]，赵洪运[1,2]，许欣欣[2]，孙广达[1,2]，周　利[1,2]，赵慧慧[3]，刘会杰[1]
(1. 哈尔滨工业大学 先进焊接与连接国家重点实验室，黑龙江 哈尔滨 150001)
(2. 哈尔滨工业大学(威海) 山东省特种焊接技术重点实验室，山东 威海 264209)
(3. 上海航天设备制造总厂有限公司，上海 200245)

摘　要：采用静轴肩搅拌摩擦焊接法（SSFSW）在不同的焊接速度下制备了2A14-T4铝合金T形接头。在优化的焊接工艺参数下，可以得到光滑的T形接头焊缝表面。结果表明：焊接熔核区（WNZ）的显微组织为完全动态再结晶产生的细小等轴晶，第2次焊核区（WNZ2）的平均晶粒尺寸最大，焊接重合区（WNOZ）次之，第1次焊核区（WNZ1）的平均晶粒尺寸最小。WNZ的再结晶机制主要是几何动态再结晶，并伴有部分连续动态再结晶。WNZ1和WNZ2织构类型为弱{111}<110>，而WNOZ经过2次搅拌后织构类型为弱{100}<001>。热机械影响区（TMAZ）发生塑性变形，而热影响区（HAZ）只受到焊接热循环作用，不发生塑性变形和晶粒的动态再结晶。WNZ的硬度较高，硬度最低的区域位于靠近TMAZ的HAZ。随着焊接速度的增加，接头抗拉伸强度先增大后减小。底板和加强板的主要断裂形式是脆性/韧性混合断裂。

关键词：2A14-T4铝合金；SSFSW；T形接头；显微组织；力学性能

作者简介：杨海峰，男，1988年生，博士生，工程师，哈尔滨工业大学先进焊接与连接国家重点实验室，黑龙江 哈尔滨 150001，电话：0631-5687196，E-mail：hf_yang@hit.edu.cn